crystals

MDPI

Article

Research on Microstructure and Cracking Behavior of Al-6.2Zn-2Mg-xSc-xZr Alloy Fabricated by Selective Laser Melting

Wei Pan [1,2,3], Ziyu Zhai [1,2,3], Yantao Liu [1,2,3], Bo Liang [1,2,3], Zhuoheng Liang [1,2,3] and Yongzhong Zhang [1,2,3,*]

[1] National Engineering & Technology Research Center for Non-Ferrous Metal Matrix Composites, GRINM Group Co., Ltd., No. 11, Xingke East Street, Yanqi Economic Development Zone, Huairou District, Beijing 101407, China
[2] GRINM Metal Composites Technology Co., Ltd., No. 11, Xingke East Street, Yanqi Economic Development Zone, Huairou District, Beijing 101407, China
[3] General Research Institute for Nonferrous Metals, No. 2, Xinjiekouwai Street, Beijing 100088, China
* Correspondence: yyzhang@grinm.com; Tel.: +86-135-0100-8631

Abstract: Selective laser melting (SLM) offers obvious advantages in the production of complex parts. However, the traditional 7xxx series aluminum alloy has a serious cracking tendency in the SLM process. Therefore, in order to analyze the microstructure and cracking mechanism, and obtain crack-free aluminum alloy fabricated by SLM, this paper studied the microstructure characteristics of as-deposited Al-6.2Zn-2Mg-xSc-xZr alloy with different Sc, Zr content, as well as the influence mechanism of Sc, Zr on cracking. The results show that with the increase of Sc and Zr content, the crack tendency and grain size decrease. When Sc and Zr content reach 0.6% and 0.36% respectively, cracks can no longer be observed in the as deposited alloy. The microstructure of the as deposited Al-6.2Zn-2Mg-0.6Sc-0.36Zr alloy consists of fine equiaxed and columnar crystals, in which Sc and Zr mainly exist in the aluminum matrix as solid solutions, and some exist in the form of Al_3(Sc, Zr). The immediate reason for the absence of cracks is that the microstructure changes from coarse columnar grains to fine equiaxed-columnar grains when the content of Sc and Zr increases. The refined grain size may have the following beneficial effects: It helps with reducing the thickness of the liquid films. This will increase the tear sensitivity of the liquid film and the cracking tendency and therefore lowers the hot cracking tendency; And a refined grain size improves fracture roughness, leading to an enhanced cracking resistance. At the same time, the refinement of the grains will make the feeding channel of the grain boundary shorter and easy to feed, and the fine equiaxed grains can coordinate stress-strain during solidification more effectively than coarse columnar grains, which will decrease the cracking tendency.

Keywords: selective laser melting; Al-Zn-Mg alloy; microstructure; cracking behavior

Citation: Pan, W.; Zhai, Z.; Liu, Y.; Liang, B.; Liang, Z.; Zhang, Y. Research on Microstructure and Cracking Behavior of Al-6.2Zn-2Mg-xSc-xZr Alloy Fabricated by Selective Laser Melting. *Crystals* **2022**, *12*, 1500. https://doi.org/10.3390/cryst12101500

Academic Editor: Shouxun Ji

Received: 7 September 2022
Accepted: 18 October 2022
Published: 21 October 2022

1. Introduction

Selective laser melting (SLM) is one of the most promising technologies in the field of metal additive manufacturing [1,2]. This technology uses a high-energy laser to melt metal powder directly, which can manufacture dense and high-performance parts [3]. SLM can fabricate complex structures that can't be processed by traditional processing methods, such as casting, forging, and mechanical machining. And it has broad application prospects in aerospace, personalized biological manufacturing, and complex molds [4,5]. Compared with traditional manufacturing processes, SLM has significant advantages in improving material utilization, manufacturing complex structural parts, shortening manufacturing cycles, and reducing manufacturing costs [6–9].

Lightweight, high-strength structural materials are pursued by modern industry [10–12]. Aluminum alloy has become the preferred material for various advanced industrial manufacturing due to the advantages of low density, high strength, and good processing

performance [13–15]. Among many aluminum alloys, 7xxx aluminum alloys are widely used in the aerospace and automobile field [16–18]. Compared with the widely used iron-based [19,20], nickel-based [21,22] and titanium-based [23,24] alloys, aluminum alloys fabricated by SLM is facing many difficulties due to the high laser reflectivity, high thermal conductivity and poor powder fluidity [25–28]. Due to the poor fluidity of the liquid 7xxx aluminum alloy, the large solidification temperature range and the rapid cooling of SLM, the serious cracking will be produced during SLM processing [29]. Kaufmann et al. [30] studied 7075 aluminum alloys manufactured by SLM with different process parameters. The results shown that all the specimens have cracks in the vertical orientation. The substrate preheating temperature of 200 °C presented no significant positive effect on reducing cracks. The high cooling rate of SLM promotes the generation of cracks. The research from Qi et al. [31] shown that when 7075 aluminum alloy was manufactured by SLM, the cracking tendency would be effectively reduced by changing the scanning speed and defocusing amount, but the cracks cannot be completely eliminated.

Otani et al. [32,33] studied the mixing 5% Si particles into 7075 alloy manufactured by SLM. The results confirmed that the Si can eliminate cracks and form fine primary grains. Zhou et al. [34] mixed Si (99.0% purity, 0.5–2 μm) and TiB2 (99.6% purity, 0.1−11 μm) particles into Al-Zn-Mg-Cu to eliminate the hot cracks. Addition of the Si alone to the Al-Zn-Mg-Cu alloy has largely reduced the macroscopic cracks, but the microcracks were still existence. But mixing two or more kinds of powders may cause uneven element distribution, which may lead to non-uniform of the mechanical properties. Aboulkhair et al. [35] believed that high-strength aluminum alloys fabricated by SLM was challenge, because aluminum alloys wound have large area cracks due to material shrinkage. Cracks wound be appeared in the final stage of solidification. And the most effective way to avoid the cracking is to change the alloy composition through pre-alloying. Zhou et al. [36] researched the Al-6Zn-2Mg alloys with 1% (Sc + Zr) addition manufactured by SLM, and a dense and crack-free microstructure was obtained. Bi et al. [37,38] designed a Sc- and Zr- modified 7075 alloy. It was analyzed that the effect of energy density on formability, microstructure and micro-hardness of Sc- and Zr- modified 7075 alloy fabricated by SLM, and the effect of energy density on spreading and solute redistribution of melt pool was investigated. Martin et al. [29] considered that the hydrogen-stabilized Zr nanoparticles in 7075 alloy resulted in the formation of Al_3Zr. Then, Al_3Zr wound be used as nucleation sites for primary aluminum during solidification, which wound produce fine equiaxed grains that inhibit the formation of microcracks.

As shown above, there are still many challenges for 7xxx series aluminum alloys fabricated by SLM [29,39], and the existing studies lacks systematic research on the microstructure and cracking mechanism. In this study, in view of the problem that Al-Zn-Mg aluminum alloy is difficult to fabricate by SLM due to crack. Sc and Zr elements were added by microalloying to reduce the cracking tendency and improve the formability and mechanical properties. The alloy composition was optimized, and the cracking mechanism of Al-Zn-Mg alloy was analyzed. The influence mechanism and law of Sc and Zr on the Al-Zn-Mg alloy were studied. This will provide theoretical support and technical solutions for Al-Zn-Mg alloys fabricated by SLM.

2. Materials and Methods

2.1. Materials Composition

For the traditional Al-Zn-Mg aluminum alloy, the Sc and Zr are mainly to form the primary Al_3(Sc, Zr) phase as heterogeneous nucleation sites to achieve the effect of grain refinement [40–43]. Due to the low cooling rate of casting aluminum alloy during solidification, the solid solubility of Sc and Zr was limited [44,45]. So, the addition amount of Sc and Zr in the aluminum alloy fabricated by traditional process is usually no more than 0.2%, and the ratio of Sc and Zr is often between 1:1 and 2:1 [46–48]. However, the cooling rate of SLM during the solidification was often above 10^4 K/s, which is much faster than the traditional process [49,50]. Therefore, the supersaturated solid solubility of Sc and Zr in

the aluminum alloy fabricated by SLM will be much larger than the traditional casting or other process. In order to study the cracking mechanism of Al-Zn-Mg alloy fabricated by SLM and the influence of Sc and Zr content on cracking, 4 groups of Al-Zn-Mg alloys with different contents of Sc and Zr were designed in this experiment, and the compositions are shown in Table 1. Elements other than Zn, Mg, Sc, Zr and Al are regarded as impurities.

Table 1. Designed alloys composition.

	Zn (wt.%)	Mg (wt.%)	Sc (wt.%)	Zr (wt.%)	Al (wt.%)
sample 1	6.2	2	0	0	Bal.
sample 2	6.2	2	0.2	0.12	Bal.
sample 3	6.2	2	0.4	0.24	Bal.
sample 4	6.2	2	0.6	0.36	Bal.

2.2. Al-6.2Zn-2Mg-xSc-xZr Alloys Powder

Four groups of Al-6.2Zn-2Mg-xSc-xZr alloy powders were prepared by N_2 gas atomization. The morphology of the powders is shown in Figure 1. It can be seen that the Al-6.2Zn-2Mg-xSc-xZr powders are spherical with small amount of satellite powder. This can ensure stability and uniformity of the powder bed during SLM process. The particle size distribution of different component powders is similar, mainly within 20–63 μm, as shown in Figure 2. Suitable particle size distribution is also beneficial to improve the stability and uniformity of powder spreading during the SLM process.

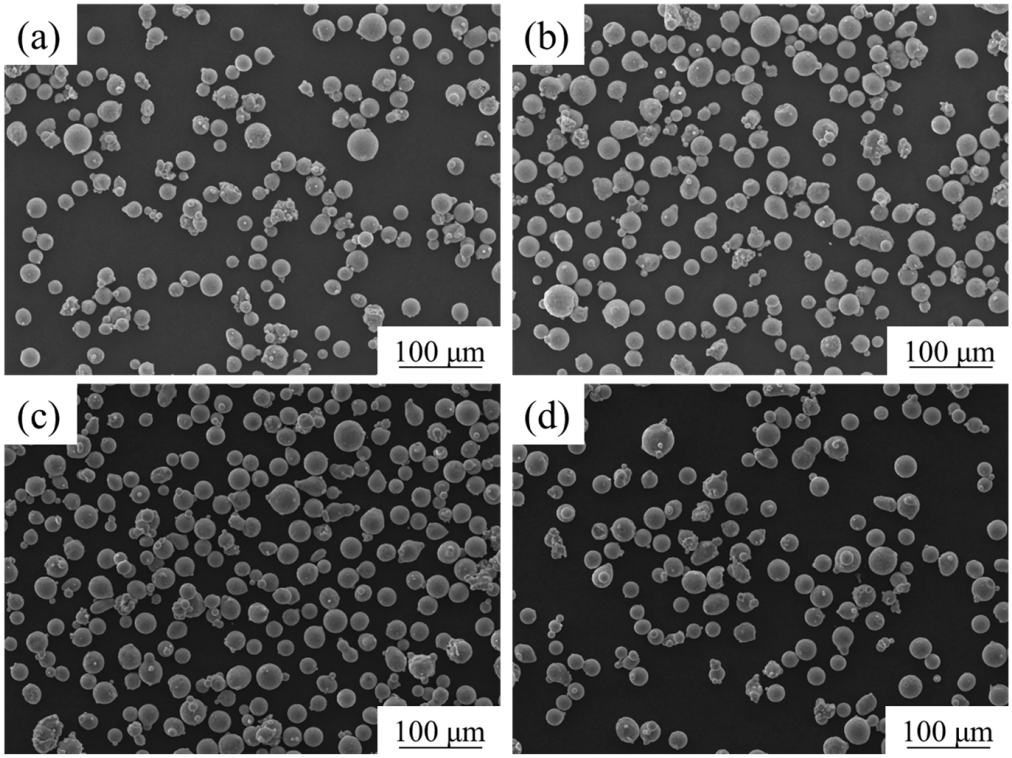

Figure 1. The morphology of Al-6.2Zn-2Mg-xSc-xZr alloys powder, (**a**) sample 1, (**b**) sample 2, (**c**) sample 3, (**d**) sample 4.

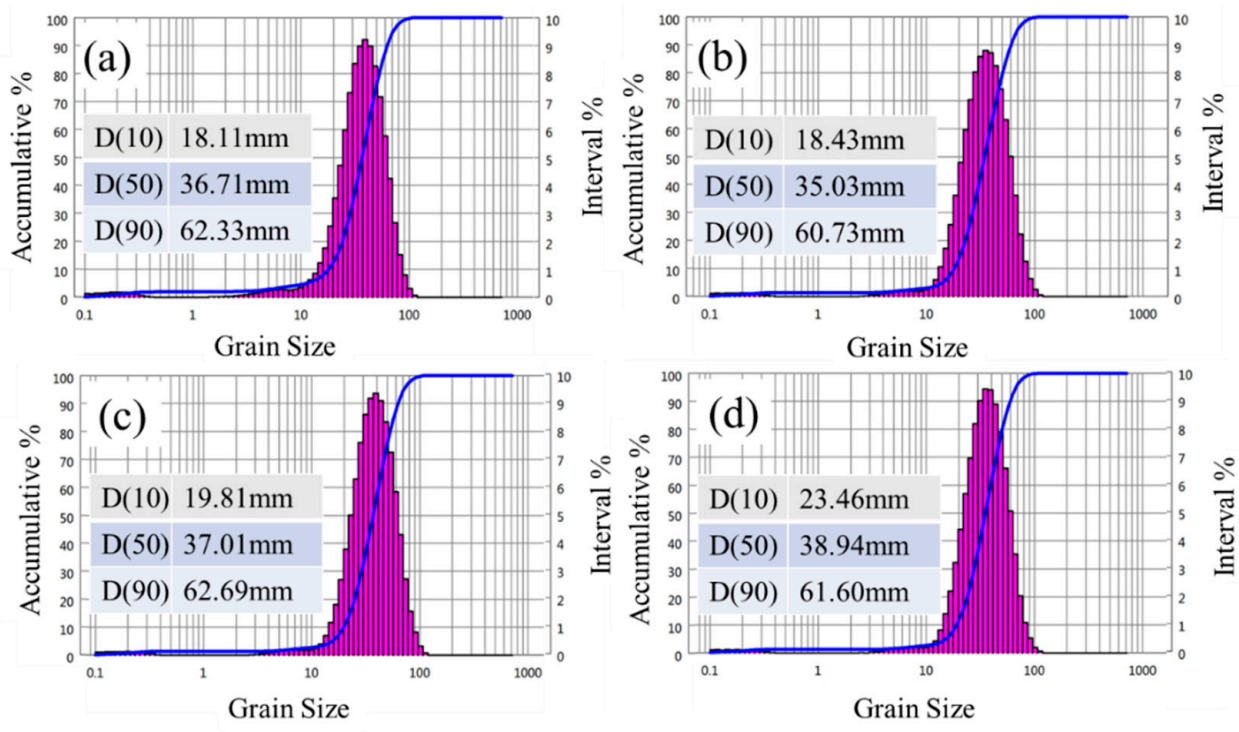

Figure 2. Particle size of Al-6.2Zn-2Mg-xSc-xZr alloys powder, (**a**) sample 1, (**b**) sample 2, (**c**) sample 3, (**d**) sample 4.

2.3. Experimental Details

In this experiment, the EP-M250 metal 3D printer (Beijing Eplus3D Technology Co., Ltd., Beijing, China) was used, and it's equipped with a 500W fiber laser. Before SLM processing. The 3D data model of the sample was firstly designed and sliced with the software, and then the process parameters were set up by the software of Ephath (Beijing Eplus3D Technology Co., Ltd.). Finally, it was imported into the EP-M250 metal 3D printer for the SLM processing. According to previous experiments, the process parameters was that the hatch spacing was 0.1 mm, the scanning speed was 841–921 mm/s, the laser power was 290 W and the layer thickness was 0.03 mm. Before processing, the powder needs to be vacuum-dried at 100 °C for at least 6 h. The oxygen content in the chamber of 3D printer is strictly controlled below 100 ppm by filling with Ar gas to prevent oxidation. After SLM processing, wire cutting was used to cut the sample. The samples analyzed by OM and SEM were polished with metallographic sandpaper, until the surface has no obvious scratches. Then the mechanical or electrolytic polishing was carried out, and the metallographic samples was corroded with Keller's etchant (2.5% HNO_3, 1.5% HCl, 1.0% HF, 95% H_2O) for 20s. The samples were rinsed with distilled water, and the samples were observed by Axiovert 200 MAT optical microscope, JSM-7900F field emission scanning electron microscope and FEI Tecnai F20 transmission electron microscope. According to the results of the microstructure analysis, the tensile rod of sample 3 and sample 4 was fabricated, and the room temperature tensile test was carried out by the Quasar10 tensile testing machine. The test standard was GB/T 228.1-2010. The surface of tension fracture was observed by SEM.

It can be seen from Figure 3, the surface of the Al-Zn-Mg sample fabricated by SLM was relatively flat, and no obvious macro cracks were observed on the surface. This shows that the Al-Zn-Mg alloy powder has good processability with suitable processing parameters. Figure 4 shows the schematic diagram of horizontal section and vertical section, blanks of tensile rods, tensile rod and its schematic diagram.

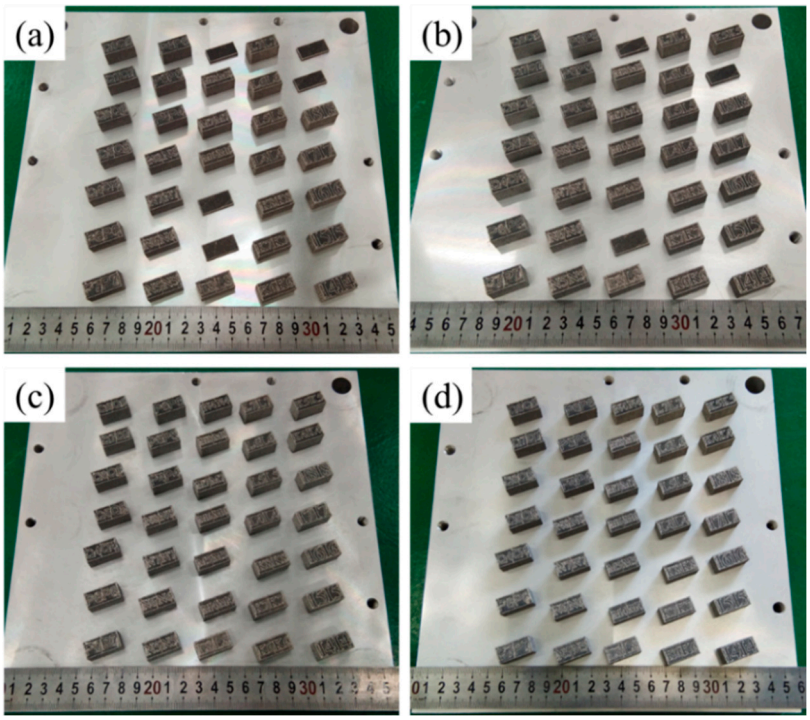

Figure 3. Al-6.2Zn-2Mg-xSc-xZr alloy sample fabricated by SLM, (**a**) sample 1, (**b**) sample 2, (**c**) sample 3, (**d**) sample 4.

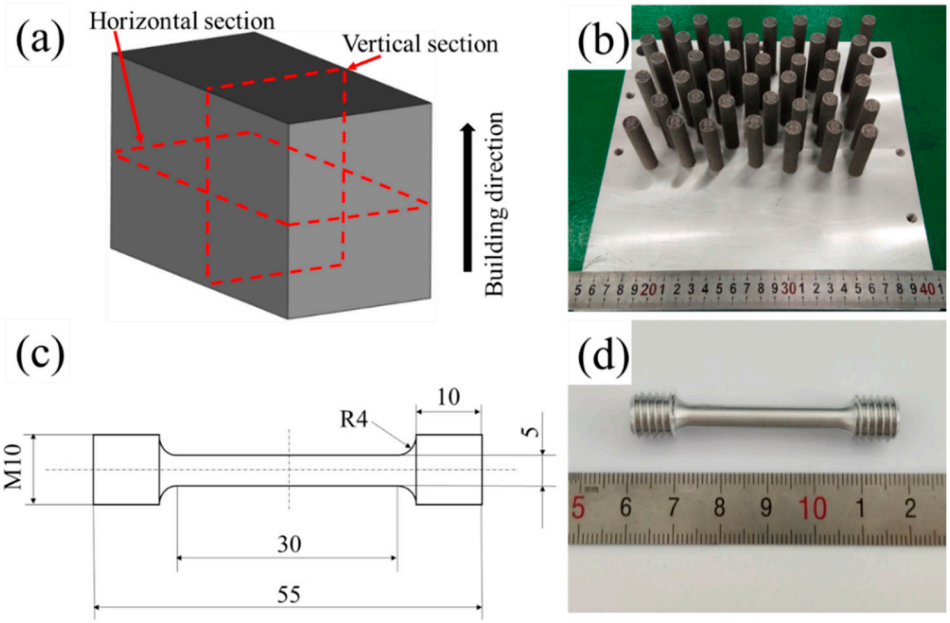

Figure 4. (**a**) schematic diagram of horizontal section and vertical section, (**b**) the blanks of tensile rods, (**c**) schematic diagram of dog-bone rod-shaped standard tensile specimen, (**d**) dog-bone rod-shaped standard tensile specimen.

3. Results

3.1. Microstructure of Al-6.2Zn-2Mg-0.6Sc-0.36Zr Alloy

Figures 5 and 6 show the metallographic microstructure and EBSD analysis of the horizontal section and the vertical section of sample 4 in the as-printed status, respectively. According to Figures 5 and 6, the microstructure is mainly composed of micron-scale grains, and a certain amount of nanograins. The microstructure is alternating columnar

and equiaxed crystals. The grain size distribution is obvious uneven, and the equiaxed crystals at the bottom of the molten pool are much smaller than the columnar crystals in the middle region of the molten pool. Figure 7 is the ECC photo of sample 4 in the as-printed status. Figure 8 shows the TEM analysis of sample 4. It can be seen from Figures 7–9 that there is a large amount of η′ phase and a small amount of Al_3(Sc, Zr) phase in the sample 4.

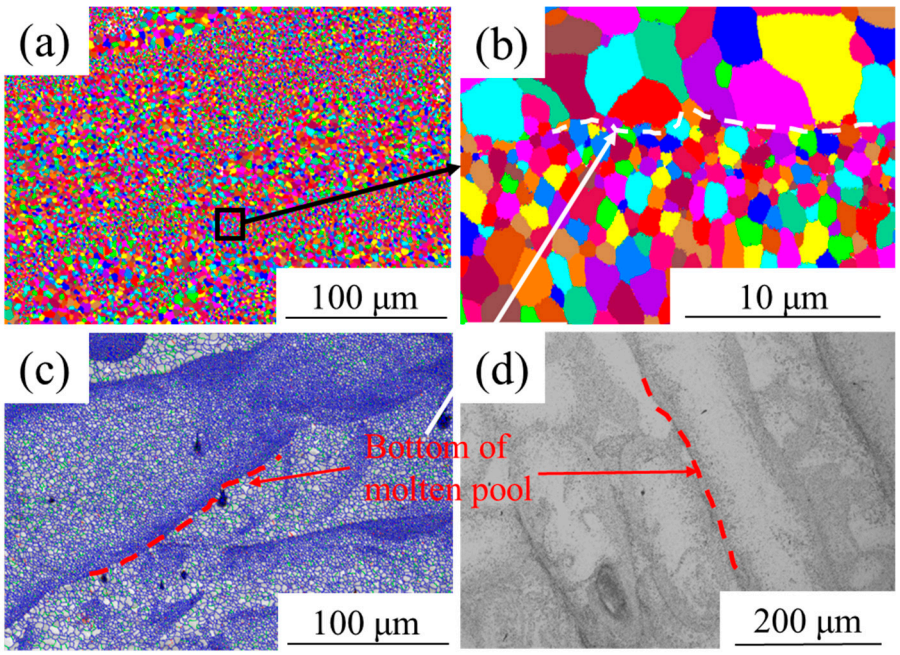

Figure 5. The metallographic structure and EBSD analysis of the horizontal section of sample 4 in the as-printed status, (**a**) grain reconstruction map, ×400, (**b**) grain reconstruction map, ×5000, (**c**) grain boundary reconstruction map, (**d**) metallographic photograph.

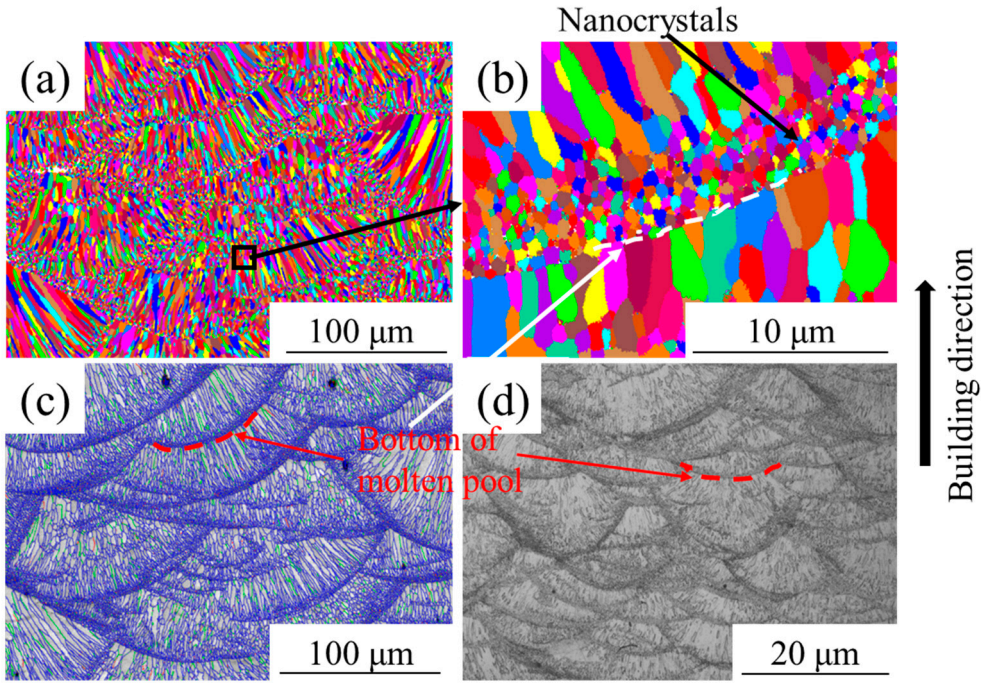

Figure 6. The metallographic structure and EBSD analysis of the vertical section of sample 4 in the as-printed status, (**a**) grain reconstruction map, ×400, (**b**) grain reconstruction map, ×5000, (**c**) grain boundary reconstruction map, (**d**) metallographic photograph.

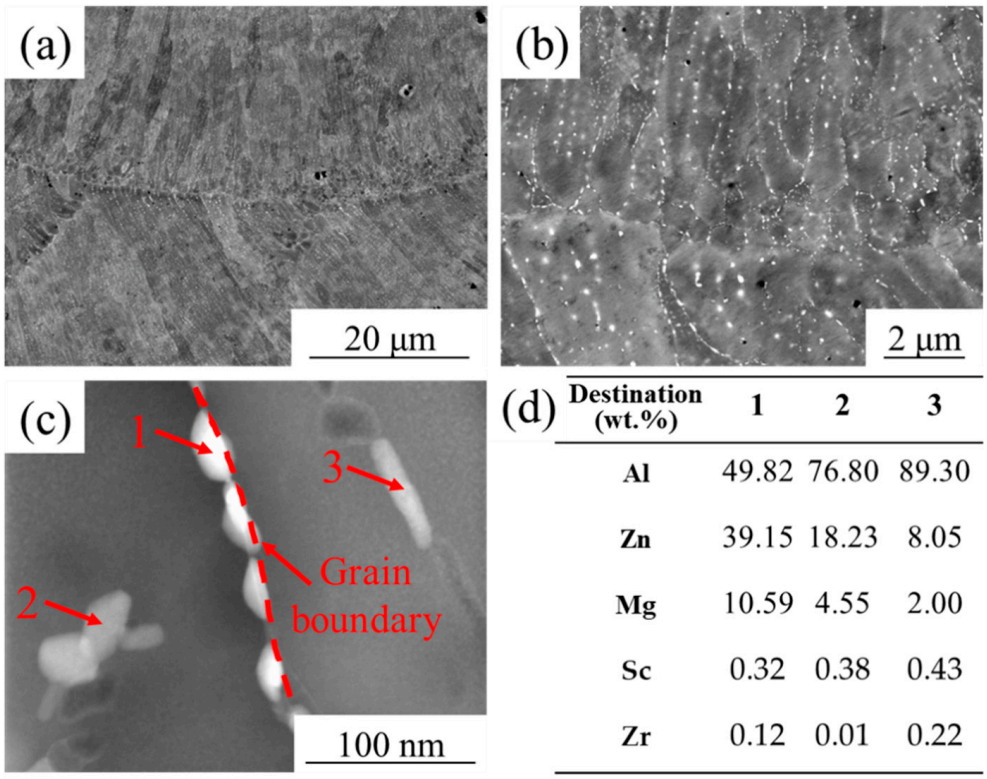

(d)

Destination (wt.%)	1	2	3
Al	49.82	76.80	89.30
Zn	39.15	18.23	8.05
Mg	10.59	4.55	2.00
Sc	0.32	0.38	0.43
Zr	0.12	0.01	0.22

Figure 7. (**a**) the ECC photo of sample 4 in the as-printed status, ×2000, (**b**) the ECC photo of sample 4 in the as-printed status, ×10,000, (**c**) TEM photo of sample 4 in as-printed status, (**d**) the EDS analysis of (**c**).

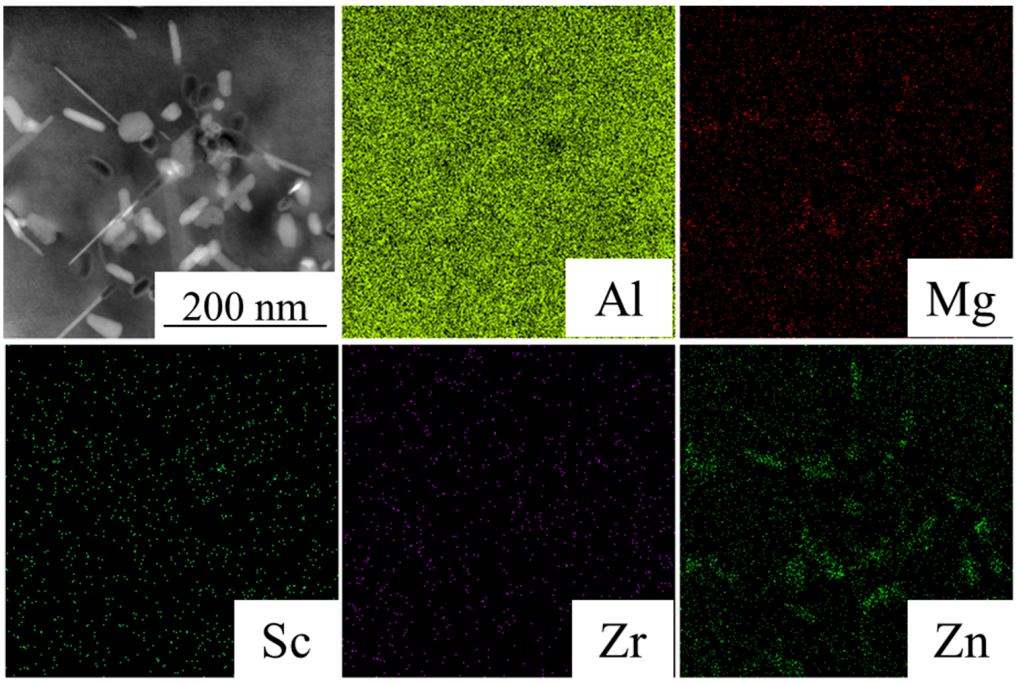

Figure 8. The TEM-EDS analysis of sample 4 in the as-printed status.

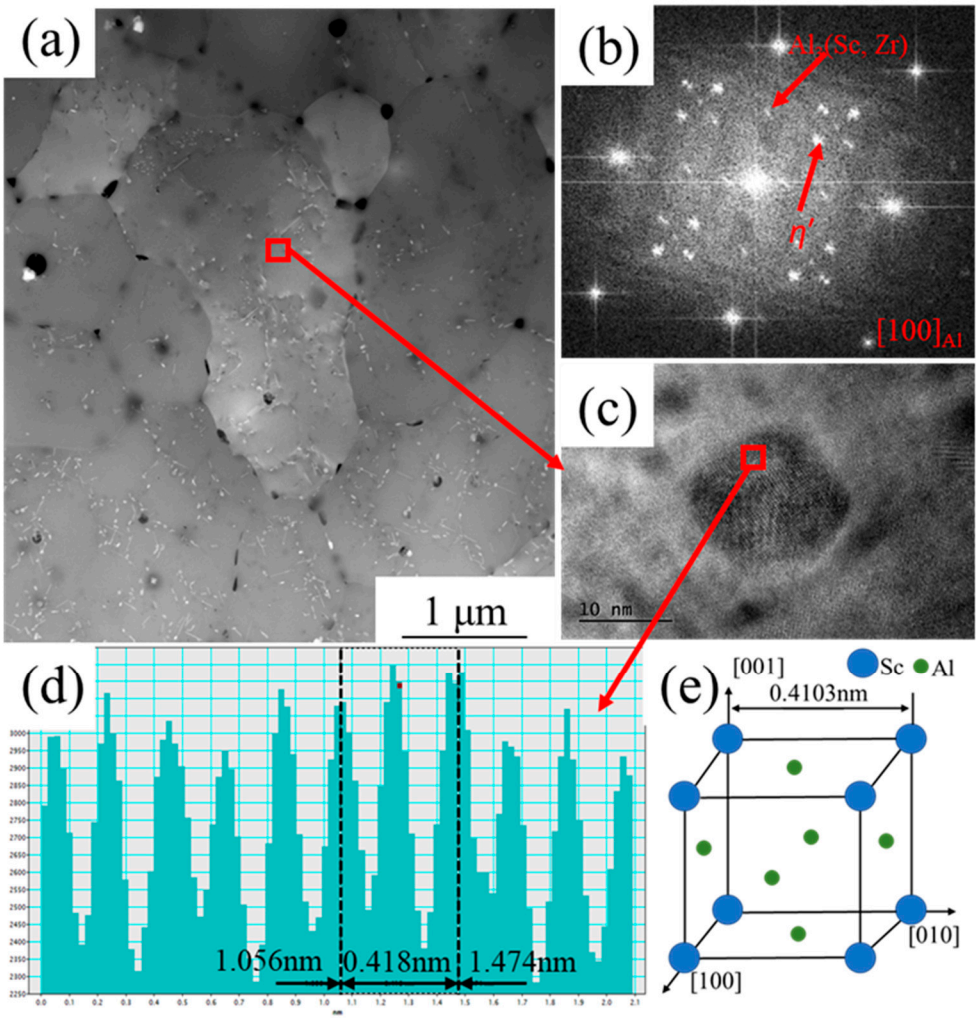

Figure 9. The TEM analysis of sample 4 in the as-printed status, (**a**) BT-TEM, (**b**) FFT of (**c**), (**c**) HRTEM, (**d**) interatomic distance measurement results, (**e**) schematic diagram of the lattice of Al_3Sc [51].

3.2. Microstructure and Mechanical Property of Al-6.2Zn-2Mg-xSc-xZr Alloys

Figure 10 shows the metallographic photos of the Al-6.2Zn-2Mg-xSc-xZr alloy samples fabricated by SLM in the horizontal directions. It can be seen that there are obvious cracks and pores in the microstructure of the sample 1 and sample 2. With the increase of Sc and Zr content, the number of cracks in the sample 3 are decreased significantly. When the content of Sc and Zr are 0.6% and 0.36% respectively, there is no cracks appeared. It indicates that the generation of cracks can be completely and effectively inhibited when the content of Sc and Zr are 0.6% and 0.36% respectively. And the microstructure with no cracks and less pores can be obtained.

Figures 11 and 12 shows the EBSD analysis of the vertical directions of Al-6.2Zn-2Mg-xSc-xZr alloy samples. When the content of Sc and Zr are equal or lower than 0.2% and 0.12% respectively, a large number of cracks that grow along the grain boundary will appear in the microstructure. And the microstructure is entirely composed of coarse columnar crystal. As the content of Sc and Zr increases, the grain size and pores decreased. When the content of Sc and Zr were 0.6% and 0.36% respectively, the microstructure shows an alternating distribution of equiaxed and columnar crystals, and the grain size is significantly smaller than that of the sample 1 and sample 2. And there were no cracks and only a small amount of pore.

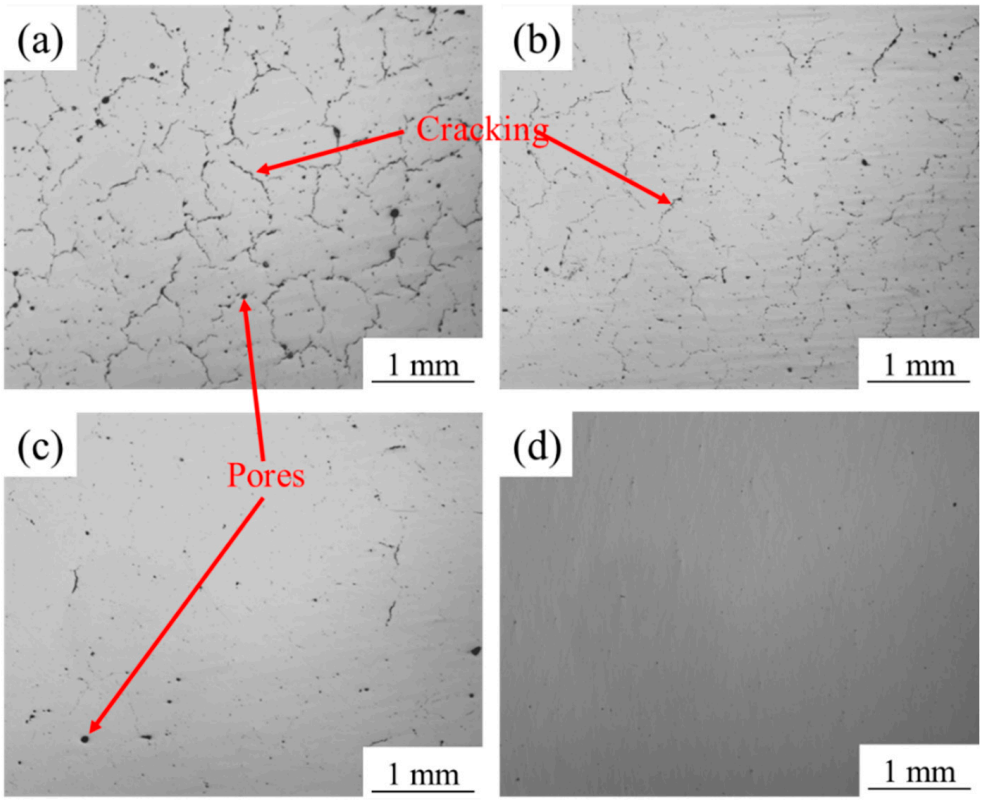

Figure 10. Horizontal microstructure morphology of Al-6.2Zn-2Mg-xSc-xZr alloy samples, (**a**) sample 1, (**b**) sample 2, (**c**) sample 3, (**d**) sample 4.

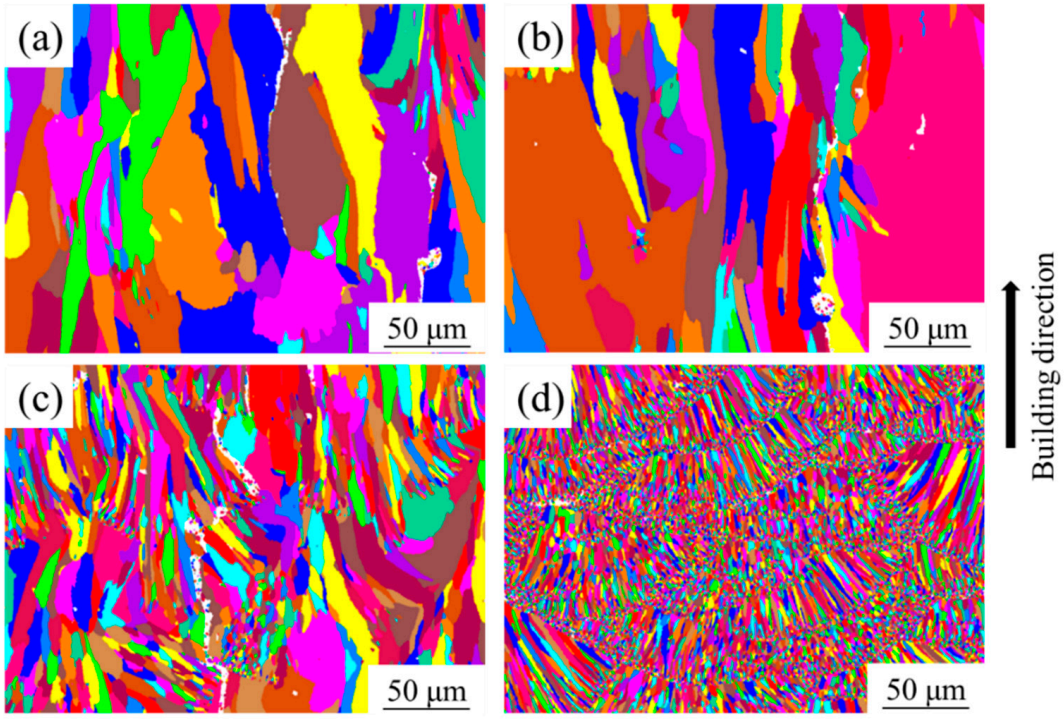

Figure 11. EBSD analysis of Al-6.2Zn-2Mg-xSc-xZr alloy samples, (**a**) sample 1, (**b**) sample 2, (**c**) sample 3, (**d**) sample 4.

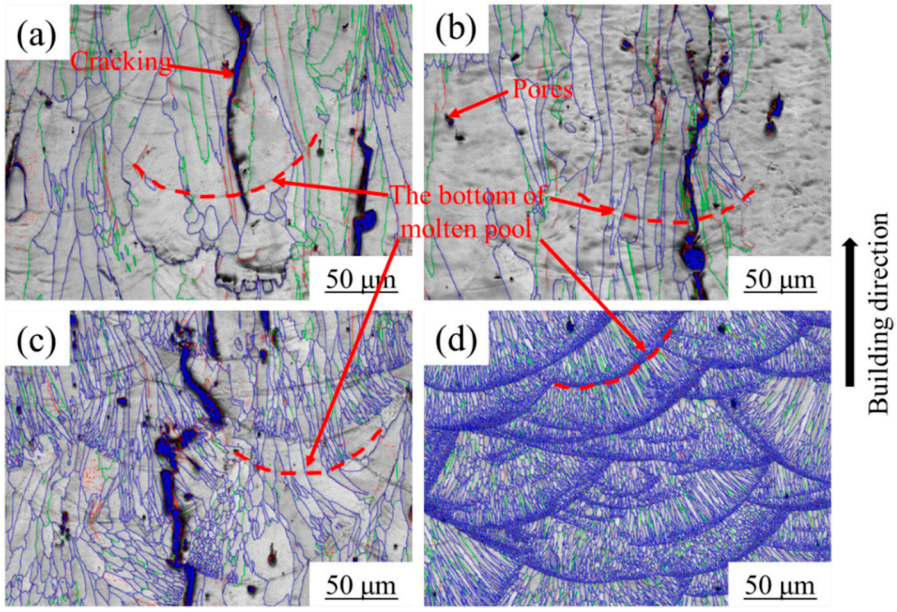

Figure 12. Grain boundary reconstruction corresponding to the Figure 11, (**a**) sample 1, (**b**) sample 2, (**c**) sample 3, (**d**) sample 4.

3.3. Mechanical Properties of Al-6.2Zn-2Mg-xSc-xZr Alloys

Due to the serious cracking of sample 1 and sample 2, only sample 3 and sample 4 were tensile tested. Table 2 shows the as-printed status mechanical properties of sample 3 and sample 4, and Figure 13 shows the corresponding histogram. Compared with sample 4, the sample 3 has lower mechanical properties due to the lower content of Sc and Zr, cracks and more pores. Figure 14 shows the tensile fracture surface of Al-6.2Zn-2Mg-xSc-xZr alloys.

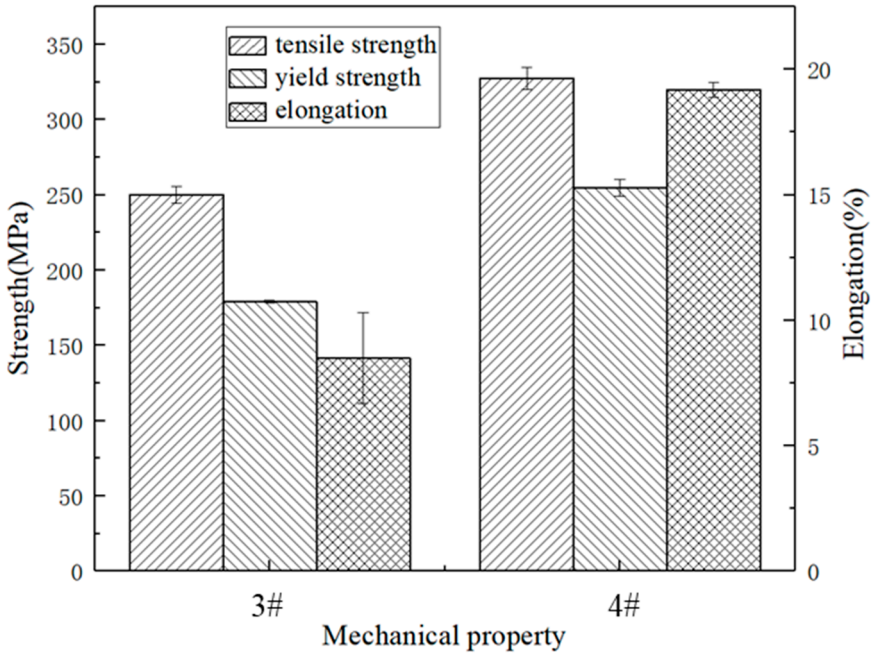

Figure 13. Mechanical properties of the as-printed Al-6.2Zn-2Mg-xSc-xZr alloys.

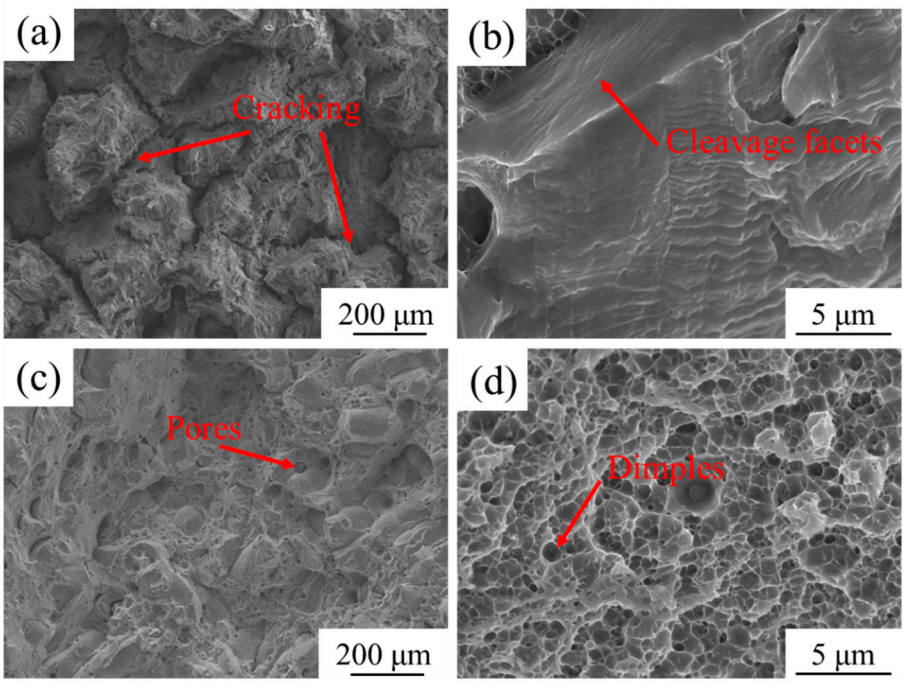

Figure 14. SEM morphology of tensile fracture surface of the as-printed Al-6.2Zn-2Mg-xSc-xZr alloy, (**a**) sample 3, (**b**) sample 3, (**c**) sample 4, (**d**) sample 4.

Table 2. Mechanical properties of the as-printed Al-6.2Zn-2Mg-xSc-xZr alloys.

No.	Ultimate Tensile Strength/MPa	Yield Strength/MPa	Elongation/%
Sample 3	250.0 ± 5.3	179.0 ± 1.0	8.5 ± 1.8
Sample 4	327.3 ± 7.1	254.7 ± 5.5	19.2 ± 0.3

4. Discussion

4.1. Microstructure Analysis of Al-6.2Zn-2Mg-0.6Sc-0.36Zr Alloy

There are two main forms of Sc and Zr in the Al-Zn-Mg alloy processed by traditional technology [44,45]. When the addition amount of Sc and Zr is less than the solid solubility, it's mainly dissolves into the Al matrix to form a solid solution. And when the addition amount exceeds the solid solubility, the supersaturated solid solution and Al_3(Sc, Zr) primary phase will be formed. Robson [52] characterized the distribution of Sc and Zr in direct chill cast 7050 alloy ingots containing Sc and Zr using an electron microprobe analyzer, and found that almost half of the Sc existed in the form of primary phase, leaving an average concentration of 0.18 wt% Sc in solid solution. Due to the high cooling rate (>10^4 K/s) of SLM [49,50], the solubility of Sc and Zr in the supersaturated solid solution will be much higher than the traditional processing techniques such as casting with low cooling rate. Therefore, the Sc and Zr in the sample 4 in the as-printed status mainly exist in the form of supersaturated solid solutions. The supersaturated solid solution will decompose and precipitate fine and dispersed $A1_3$(Sc, Zr) particles after heat treatment, which have a significant precipitation strengthening effect on aluminum alloys.

Figure 7a,b are the ECC picture of the Al-6.2Zn-2Mg-0.6Sc-0.36Zr alloy in the as-printed status. The Mg/Zn-rich nanoscale phases have a certain degree of aggregation at the grain boundaries. This indicates that the diffusion of elements is restricted under rapid cooling of SLM processing. However, due to the disordered arrangement of atoms at the grain boundary, the energy of the grain boundary increases, which provides the necessary driving force for the precipitation of the second phase. Figures 8 and 9 show the TEM photo and selected area electronic diffraction analysis of the Al-6.2Zn-2Mg-0.6Sc-0.36 Zr alloy. It can be seen that the second phase is mainly the η′ phase according to Figures 7–9 [53–55].

Fine grain strengthening and precipitation strengthening of Mg/Zn phase play a major role in strengthening of the Al-6.2Zn-2Mg-0.6Sc-0.36Zr alloys. As shown from Figure 9b, there were the obvious diffraction points appear at the [1 0 0] and [1 1 0] positions in the diffraction pattern of the $[1\ 0\ 0]_{Al}$ crystal belt axis. In the high-resolution electron microscope pictures (Figure 9c), a lattice arrangement different from the Al matrix phase was found. The measurement and calculation of the lattice in this area confirmed that the spacing of the interphase atomic columns was about 0.418 nm (Figure 9d). It is similar to the Al_3Sc lattice parameter of 0.4103 nm [51]. And it is matched with the schematic diagram of the Al_3Sc atomic structure shown in Figure 9e. The Al_3(Sc, Zr) is formed by the substitution of Zr atom for Sc atom of the Al_3Sc shell, and their lattice structures and lattice constants are similar. And combined with electron diffraction analysis (Figure 9b), it is determined that this phase is Al_3(Sc, Zr) with $L1_2$ structure.

In summary, when the sample 4 was manufactured by SLM, the powder was rapidly melts and solidifies during laser rapid scanning due to the small laser spot and high energy density. Even if the content of Sc and Zr in the aluminum alloy is relatively high, but no massive Al_3(Sc, Zr) primary phase is formed. Sc and Zr elements exist as the form of solid solution and nano-sized small primary Al_3(Sc, Zr) phase.

Figure 15a is the EBSD grain reconstruction of the sample 4. The microstructure is composed of fine equiaxed crystals on bottom of the molten pool, and coarse columnar crystal in the middle of the molten pool. Due to the overlap of adjacent melting pool and remelting between layers, there is no complete microstructure of the molten pool as shown in the schematic diagram (Figure 15b) inside the sample.

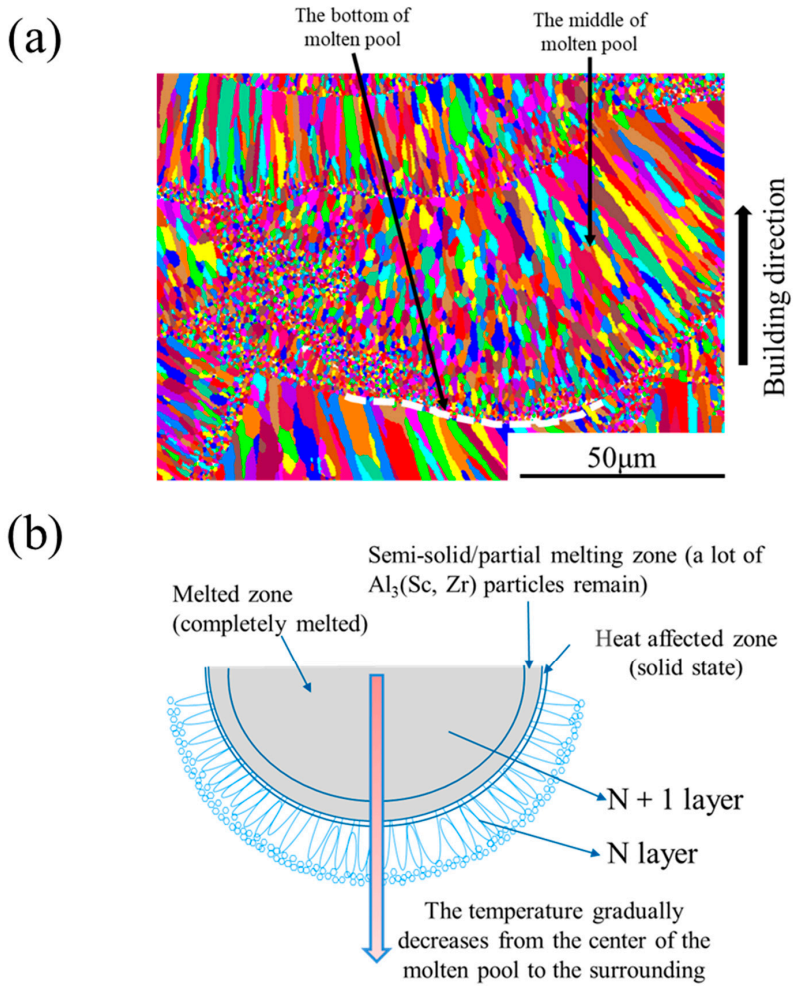

Figure 15. (**a**) EBSD grain reconstruction of the vertical plane of sample 4, (**b**) Schematic diagram of the solidification of the molten pool during the SLM process.

According to the study of J. D. Hunt [56], the number of nucleation sites plays a important role in the growth of grains, especially when there is a high thermal gradient in the bottom area of the molten pool. According to Spierings et al. [57], Al_3(Sc, Zr) particles can survive to approximately 800 °C. Therefore, due to the laser remelting to the previous layer, many Al_3(Sc, Zr) particles remain in the semi-solid/partial melting zone at the bottom of the molten pool [58]. And due to the high Sc, Zr content of sample 4, Al_3(Sc, Zr) particles will be preferentially precipitated from the melt during solidification. So, the Al_3(Sc, Zr) particles will act as nucleation sites to induce the formation of equiaxed crystal. Therefore, a large number of crystal nuclei can be generated at the bottom of the molten pool. These crystal nuclei grow rapidly until contacting to each other, and generating a fine-grained region at the bottom of the molten pool, as shown in Figure 15.

4.2. Effect of Sc and Zr on Al-6.2Zn-2Mg-xSc-xZr Alloys

When Sc is added to the aluminum alloy, the primary $A1_3Sc$ particles will be generated during the solidification. The crystal structure and lattice constant of tiny $A1_3Sc$ particles are very similar to the Al matrix. Therefore, the primary $A1_3Sc$ particles have good grain refinement effect. According to Hall-Petch theory, grain refinement will significantly improve alloy strength. When Sc and Zr are added together to the aluminum alloy, the phenomenon of grain refinement caused by the composite addition will be better. This is because Zr atoms can wrap around the $A1_3Sc$ phase to form the $A1_3$(Sc, Zr) phase. The lattice type and lattice parameters of $A1_3$(Sc, Zr) phase is similar to $A1_3Sc$. $A1_3$(Sc, Zr) is not only maintains the beneficial effects of $A1_3Sc$, but also it has better thermal stability than $A1_3Sc$. Al_3(Sc, Zr) particles also can effectively inhibit the recrystallization, and increase the recrystallization temperature. Compared with traditional processes such as casting, the SLM has a very high cooling rate, which can greatly increase the supersaturated solid solubility of Sc and Zr. So, four kinds of aluminum alloy powders with different content of Sc and Zr were prepared, and the highest content of Sc and Zr was nearly 1% which is much higher than the amount added in traditional processes.

As shown in Figures 10 and 11, when the content of Sc and Zr in the alloy was 0%, the sample 1 has obvious cracks that grow along the grain boundary, accompanied by larger pores. And the size of most columnar crystal was above 100 μm. The grains passed through the bottom of molten pool and shown obvious epitaxial growth. The reason is that the liquid metal always keeps in contact with its homogeneous solid-phase substrate during the solidification of the molten pool. And compared with the nucleation in the molten pool, the solid-phase substrate provides a good epitaxial growth substrate. And due to the high temperature gradient of the molten pool, the nucleation undercooling at the interface between the molten pool and the substrate is the lowest. Therefore, when there is no preferential precipitation of heterogeneous nucleation sites in front of the interface between the molten pool and the substrate, the microstructure of SLM-fabricated alloy is usually epitaxially grown directly from the substrate, showing the characteristics of directional columnar crystals growth along the temperature gradient. Its typical macroscopic grain microstructure is epitaxially grown columnar grain structure. When the content of Sc and Zr were 0.20% and 0.12% respectively, the microstructure also appears larger cracks. Grain size and crack size have no significant changes compared with sample 1 without Sc and Zr. This shows that when a small amount of Sc and Zr was added, the Sc and Zr elements have no obvious effect on the grain refinement and reducing cracking tendency. The essence of phase precipitation is the process of element diffusion and aggregation. Due to that the SLM processing has a high cooling rate (>10^4 K/s), small amount of Sc and Zr can't effectively precipitate as heterogeneous nucleation sites in front of the interface between molten pool and Al substrate to refine grains in a very short time. However, it exists in the form of solid solution in the aluminum matrix.

When the content of Sc and Zr were 0.40% and 0.24% respectively, the grain size was different, and the grain refinement was obvious compared with sample 1 and sample 2. There are a few small equiaxed crystals at the bottom of the molten pool, and the number

and size of cracks are significantly reduced. And there is no obvious epitaxial growth of large columnar crystals. This shows that when the Sc and Zr is 0.40% and 0.24% respectively, a part of the Sc and Zr were precipitated as heterogeneous nucleation sites in front of the interface between molten pool and Al substrate, which refined the grains and hindered the epitaxial growth of columnar grains. The other Sc and Zr were in the form of solid solution existed in the aluminum matrix. Compared with sample 1 and sample 2, the increase of Sc and Zr significantly reduces the cracking tendency. When the content of Sc and Zr were 0.60% and 0.36% respectively, the grains were further refined. The high density of Sc and Zr atoms in the molten pool provided a sufficient condition for the large precipitation of $A1_3$(Sc, Zr) in a short time. And it appears as a typical alternating distribution of fine equiaxed crystals at the bottom of the molten pool and relatively coarse columnar crystals in the middle of the molten pool. The equiaxed crystals at the bottom of the molten pool reach the nano-level. No cracks were found. Compared with sample 3, the increase of Sc and Zr leads to more precipitation of $A1_3$(Sc, Zr) phase as heterogeneous nucleation sites, which can achieve better effect of grain refinement. And the increase of Sc and Zr can effectively inhibit the cracking tendency.

Due to the obvious cracking behavior of the samples when the content of Sc and Zr were low, only the sample 4 without cracks and the sample 3 with few cracks were carried out the tensile test. As shown in Table 2 and Figure 13, the tensile strength of the sample 4 is 327.3 ± 7.1 MPa, the yield strength is 254.7 ± 5.5 MPa, and the elongation is 19.2 ± 0.3%. The tensile strength of the sample 3 is 250.0 ± 5.3 MPa, yield strength is 179.0 ± 1.0 MPa, and the elongation is 8.5 ± 1.8%. Although the mechanical properties of the sample 3 are relatively low, it has stable performance and good plasticity. It is mainly due to the fact that there are fewer cracks in its microstructure, and the cracking direction is the same as the tensile direction. As shown in Figures 5 and 6, the grains of sample 4 are fine, and some of grains are nano-sized. According to the Hall-Patch formula:

$$\sigma_s = \sigma_0 + kd^{-1/2} \quad (1)$$

where σ_s is a constant which is roughly equivalent to the yield strength of a single crystal, and K is a constant which represents the degree of influence of grain boundaries on strength. The smaller the grains, the higher the yield strength. When the grains are plastically deformed, the smaller the grains, the smaller the distance from the dislocation source on the slip surface to the grain boundary. And the smaller number of packed dislocations, the lower the stress concentration caused. In addition, when the grain size is small, the difference of the degree of strain between inside the grain and the vicinity of the grain boundary is small, which will make the grains deformation is more uniform. So, there is more difficult to crack due to stress concentration, and the sample 4 has better plasticity. As shown in Figure 13, the fracture surface of the sample 4 is a micron-scale dimple-like morphology, which is one of the reasons for its good mechanical properties. Obvious cracks can be observed on the fracture surface of the sample 3. The fracture surface is composed of many cleavage steps and a small amount of micron-level dimple-like structure. This is a brittle-ductile mixed fracture. The existence of cracks, massive pores and coarse grains determine that the mechanical properties of the sample 3 is significantly lower than those of the sample 4. Compared to Zhu's studies [39], the strength of the sample 4 is relatively low. This is mainly due to the difference in composition, especially the difference in the content of Cu, which has a strengthening effect for 7xxx aluminum alloy. And improving the mechanical properties of the samples is one of the directions of our follow-up experiments.

4.3. Cracking Behavior Analysis of Al-6.2Zn-2Mg-xSc-xZr Alloys

Cracking behavior is associated with shrinkage at the liquid-to-solid transition. Near the final stage of solidification, the solute-rich melt will be highly unstable and supercooled, which will produce the grain boundaries with a thin layer of trapped liquid and mushy zone. For Al-Zn-Mg alloy, the low melting point phase rich in Zn and Mg would be aggregated at the grain boundary (e.g., Figure 7). When the sample 1 and sample 2 were

fabricated by SLM, a thin and continuous semi-solid/liquid film rich in low melting point phase was formed between adjacent massive columnar grains. And due to the large size of the semi-solid/liquid film between the grains and the high cooling rate of the SLM, the feeding between the grains was limited, and the mushy zone between the grains would crack by the shrinkage stress.

As shown in Figure 11, the microstructures of sample 1 and sample 2 was long columnar grains along the build direction, which corresponds to the thermal gradient direction. These large columnar grains spanned over at least two to three powder layers, and the exhibited significant epitaxial growth. Compared to fine equiaxed and columnar crystals, these coarse columnar grains were not sufficient to coordinate the tensile strains generated during solidification. These tensile stresses would tear the mushy melt between grains, and leading to cracks.

The epitaxial tendency of crack growth was largely due to the poor flowability of molten Al-Zn-Mg alloy and the high cooling rate of the SLM, which would lead to the inability of the molten alloy of current layer to refill pre-existing cracks [59]. If the pre-existing crack is not replenished by molten alloy, it would act as a source for further crack propagation to form a large crack, as shown in Figure 12. So, the sample 4 is completely no cracking, which mainly be due to the effect of grain refining.

Therefore, it can be seen from Figures 11 and 12 that the grains of sample 1 without Sc and Zr elements is coarse compared with sample 4 with 0.6% Sc and 0.36% Zr. The grain size in the vertical direction far exceeds the powder thickness of 30 μm per layer during SLM processing. The crack is mainly distributed along the grain boundary direction. The immediate reason for the absence of cracks is that the microstructure changes from coarse columnar grains to fine equiaxed-columnar grains when the content of Sc and Zr increases. The length of grain boundaries is greatly increased and the grain boundary feeding channel become greatly shorter, which will lead to easy to feeding, as shown in Figure 16a. At the same time, the refined grain size may have the following beneficial effects: It helps with reducing the thickness of the liquid films. This will increase the tear sensitivity of the liquid film and the cracking tendency and therefore lowers the hot cracking tendency. This was confirmed by the study of Sigworth [60]; And a refined grain size improves fracture roughness, leading to an enhanced cracking resistance [61]. In addition, the fine equiaxed grains can coordinate stress-strain during solidification more effectively than coarse columnar grains to reduce the cracking tendency.

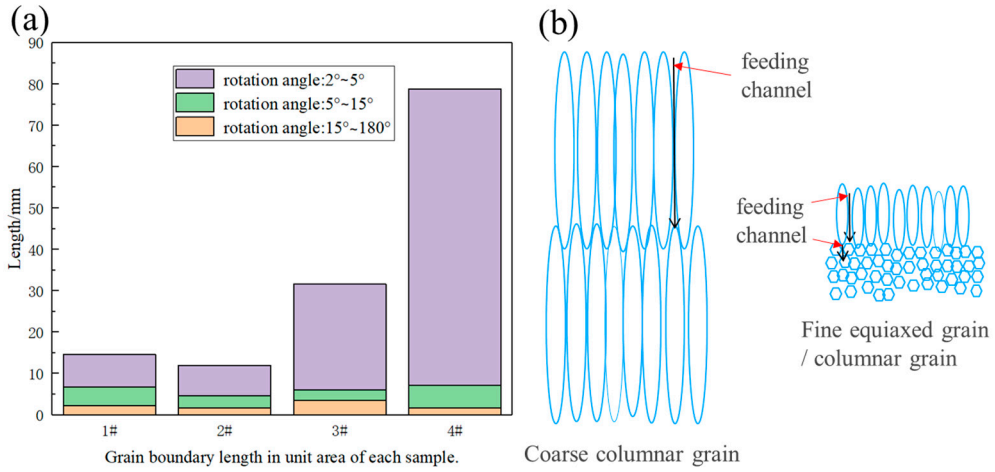

Figure 16. (**a**) Grain boundary length in unit area corresponding Figure 12, (**b**) Schematic diagram of grain boundary feed channel changes after refinement.

5. Conclusions

In this experiment, the microstructure and cracking mechanism of Al-6.2Zn-2Mg-xSc-xZr alloy manufactured by SLM were studied, and the following conclusions were obtained:

1. For the Al-6.2Zn-2Mg-xSc-xZr alloy, with the increase of Sc and Zr content from 0 and 0 to 0.6% and 0.36% respectively, the microstructure changes from coarse epitaxial growth columnar grains to fine equiaxed and columnar grains. And the cracking tendency gradually decreases until there is no crack at all. The addition of Sc and Zr can significantly refine the grains and reduce the cracking tendency.
2. The precipitated phase of Al-6.2Zn-2Mg-0.6Sc-0.36Zr alloy in the as-printed status is mainly Mg/Zn phase. Sc and Zr are mainly dissolved in aluminum matrix. A small part of Sc and Zr exists in the form of fine Al3(Sc, Zr) phase, and there is no coarse Al3(Sc, Zr) phase. The primary Al3(Sc, Zr) phase can not only serve as the heterogeneous nucleation sites of the current layer to refine the grains, but also act as the nucleation particle in the subsequent layer to induce the formation of fine equiaxed grains. But when the content of Sc and Zr is 0.2% and 0.12% respectively, Sc and Zr cannot be effectively precipitated in the form of Al3(Sc, Zr) phase as heterogeneous nucleation sites to refine grains due to the high cooling rate of SLM.
3. The immediate reason for the absence of cracks is that the microstructure changes from coarse columnar grains to fine equiaxed-columnar grains when the content of Sc and Zr increases. The refined grain size may have the following beneficial effects: It helps with reducing the thickness of the liquid films. This will increase the tear sensitivity of the liquid film and the cracking tendency and therefore lowers the hot cracking tendency; And a refined grain size improves fracture roughness, leading to an enhanced cracking resistance. At the same time, the refinement of the grains will make the feeding channel of the grain boundary shorter and easy to feed, and the fine equiaxed grains can coordinate stress-strain during solidification more effectively than coarse columnar grains, which will decrease the cracking tendency.

Author Contributions: W.P.: Conceptualization, Methodology, Software, Investigation, Writing-original draft, Writing-review & editing, Visualization, Formal analysis. Z.Z.: Investigation, Formal analysis. Y.L.: Writing-review & editing, Resources. B.L.: Resources. Z.L.: Writing-review & editing. Y.Z.: Validation, Supervision, Writing-review & editing, Resources, Project administration. All authors have read and agreed to the published version of the manuscript.

Funding: This research received no external funding.

Data Availability Statement: Date is contained within the article.

Acknowledgments: The financial support by GRINM Metal Composites Technology Co., Ltd. and research platform support by National Engineering & Technology Research Center for Non-ferrous Metal Matrix Composites, GRINM Group Co., Ltd. is greatly acknowledged.

Conflicts of Interest: The authors declare no conflict of interest.

References

1. Herzoga, D.; Seydab, V.; Wyciskb, E.; Emmelmannab, C. Additive manufacturing of metals. *Acta Mater.* **2016**, *117*, 371–392. [CrossRef]
2. Wang, X.J.; Zhang, L.C.; Fang, M.H.; Sercombe, T.B. The effect of atmosphere on the structure and properties of a selective laser melted Al-^{12}Si alloy. *Mater. Sci. Eng. A* **2014**, *597*, 370–375. [CrossRef]
3. Hooper, P. Melt pool temperature and cooling rates in laser powder bed fusion. *Acta Mater.* **2018**, *22*, 548–559. [CrossRef]
4. DebRoy, T.; Wei, H.L.; Zuback, J.S.; Mukherjee, T.; Elmer, J.W.; Milewski, J.O.; Beese, A.M.; Wilson-Heid, A.; De, A.; Zhang, W. Additive manufacturing of metallic components—Process, structure and properties. *Prog. Mater. Sci.* **2018**, *92*, 112–124. [CrossRef]
5. Tofail, S.A.M.; Koumoulos, E.P.; Bandyopadhyay, A.; Bose, S.; O'Donoghue, L.; Charitidis, C. Additive manufacturing: Scientific and technological challenges, market uptake and opportunities. *Mater. Today* **2018**, *21*, 22–37. [CrossRef]
6. Kotadia, H.R.; Professora, A.; Gibbonsa, G.; Dasb, A.; Howes, P.D. A review of Laser Powder Bed Fusion Additive Manufacturing of aluminium alloys: Microstructure and properties. *Addit. Manuf.* **2021**, *46*, 102155. [CrossRef]
7. Demir, A.G.; Previtali, B. Additive manufacturing of cardiovascular CoCr stents by selective laser melting. *Mater. Des.* **2017**, *119*, 338–350. [CrossRef]
8. Christian, C.R.; Thomas, T.-D.; Dirk, M. Plasticity and fracture of cast and SLM AlSi10Mg: High-throughput testing and modeling. *Addit. Manuf.* **2021**, *43*, 101998. [CrossRef]

9. Geng, Y.X.; Wang, Q.; Wang, Y.M.; Zang, Q.H.; Mi, S.B.; Xu, J.H.; Xiao, Y.K.; Wu, Y.; Luan, J.H. Microstructural evolution and strengthening mechanism of high-strength AlSi8.1Mg1.4 alloy produced by selective laser melting. *Mater. Des.* **2022**, *218*, 110674. [CrossRef]
10. Hoffmann, K.G.; Haag, K.; Müssig, J. Biomimetic approaches towards lightweight composite structures for car interior parts. *Mater. Des.* **2021**, *212*, 110281. [CrossRef]
11. Zhang, H.; Yang, Y.; Hu, K.H.; Liu, B.; Liu, M.; Huang, Z.R. Stereolithography-based additive manufacturing of lightweight and high-strength Cf/SiC ceramics. *Addit. Manuf.* **2020**, *34*, 101119. [CrossRef]
12. Wang, P.; Song, J.; Nai, M.L.S.; Wei, J. Experimental analysis of additively manufactured component and design guidelines for lightweight structures: A case study using electron beam melting. *Addit. Manuf.* **2020**, *33*, 101088. [CrossRef]
13. Hirsch, J.; Al-Samman, T. Superior light metals by texture engineering: Optimized aluminum and magnesium alloys for automotive applications. *Acta Mater.* **2013**, *61*, 818–843. [CrossRef]
14. She, H.; Shu, D.; Dong, A.; Wang, J.; Sun, B.; Lai, H. Relationship of particle stimulated nucleation, recrystallization and mechanical properties responding to Fe and Si contents in hot-extruded 7055 aluminum alloys. *J. Mater. Sci. Technol.* **2019**, *35*, 2570–2581. [CrossRef]
15. Yang, Y.; Zhang, Z.; Li, X.; Wang, Q.; Zhang, Y. The effects of grain size on the hot deformation and processing map for 7075 aluminum alloy. *Mater. Des.* **2013**, *51*, 592–597. [CrossRef]
16. Yuan, L.L.; Guo, M.X.; Habraken, A.M.; Duchene, L.; Zhuang, L.Z. Extremely improved formability of Al–Zn–Mg–Cu alloys via micro-domain heterogeneous structure. *Mater. Sci. Eng. A* **2022**, *873*, 142737. [CrossRef]
17. Wang, Z.P.; Wang, M.L.; Li, Y.G.; Xiao, H.Y.; Chen, H.; Geng, J.W.; Li, X.F.; Chen, D.; Wang, H.W. Effect of pretreatment on microstructural stability and mechanical property in a spray formed Al-Zn-Mg-Cu alloy. *Mater. Des.* **2021**, *203*, 109618. [CrossRef]
18. Azarniya, A.; Taheri, A.K.; Taheri, K.K. Recent advances in ageing of 7xxx series aluminum alloys: A physical metallurgy perspective. *J. Alloys Compd.* **2019**, *781*, 945–983. [CrossRef]
19. Fang, Y.J.; Kim, M.; Zhang, Y.L.; Duan, Z.Y.; Yuan, Q.; Suhr, J. Particulate-reinforced iron-based metal matrix composites fabricated by selective laser melting: A systematic review. *J. Manuf. Process.* **2022**, *74*, 592–639. [CrossRef]
20. Cacace, S.; Semeraro, Q. Influence of the atomization medium on the properties of stainless steel SLM parts. *Addit. Manuf.* **2020**, *36*, 101509. [CrossRef]
21. Carter, L.N.; Martin, C.; Withers, P.J.; Attallah, M.M. The influence of the laser scan strategy on grain structure and cracking behaviour in SLM powder-bed fabricated nickel superalloy. *J. Alloys Compd.* **2014**, *615*, 338–347. [CrossRef]
22. Sitek, R.; Molak, R.; Zdunek, J.; Bazarnik, P.; Wiśniewski, P.; Kubiak, K.; Mizera, J. Influence of an aluminizing process on the microstructure and tensile strength of the nickel superalloy IN 718 produced by the Selective Laser Melting. *Vacuum* **2021**, *186*, 110041. [CrossRef]
23. Gu, D.D.; Hagedorn, Y.; Meiners, W.; Wissenbach, K.; Poprawe, R. Nanocrystalline TiC reinforced Ti matrix bulk-form nanocomposites by Selective Laser Melting (SLM): Densification, growth mechanism and wear behavior. *Composit. Sci. Technol.* **2011**, *71*, 1620–1621. [CrossRef]
24. Han, C.; Babicheva, R.; Chua, J.D.Q.; Ramamurty, U.; Tor, S.B.; Sun, C.; Zhou, K. Microstructure and mechanical properties of (TiB+TiC)/Ti composites fabricated in situ via selective laser melting of Ti and B4C powders. *Addit. Manuf.* **2020**, *36*, 101466. [CrossRef]
25. Olakanmi, E.O. Selective laser sintering/melting (SLS/SLM) of pure Al, Al–Mg, and Al–Si powders: Effect of processing conditions and powder properties. *J. Mater. Process. Technol.* **2013**, *213*, 1387–1405. [CrossRef]
26. Chen, H.; Chen, Y.X.; Liu, Y.; Wei, Q.S.; Shi, Y.S.; Yan, W.T. Packing quality of powder layer during counter-rolling-type powder spreading process in additive manufacturing. *Int. J. Mach. Tools Manuf.* **2020**, *153*, 103553. [CrossRef]
27. Riener, K.; Oswald, S.; Winkler, M.; Leichtfried, G.J. Influence of storage conditions and reconditioning of $AlSi_{10}Mg$ powder on the quality of parts produced by laser powder bed fusion (LPBF). *Addit. Manuf.* **2021**, *39*, 101896. [CrossRef]
28. Le, T.; Wang, X.G.; Davidson, K.P.; Fronda, J.E.; Seita, M. Experimental analysis of powder layer quality as a function of feedstock and recoating strategies. *Addit. Manuf.* **2021**, *39*, 101890. [CrossRef]
29. Martin, J.H.; Yahata, B.D.; Hundley, J.M.; Mayer, J.A.; Schaedler, T.A.; Pollock, T.M. 3D printing of high-strength aluminum alloys. *Nature* **2017**, *549*, 365–369. [CrossRef]
30. Kaufmann, N.; Imran, M.; Wischeropp, T.M.; Emmelmann, C.; Siddique, S.; Walther, F. Influence of Process Parameters on the Quality of Aluminium Alloy EN AW 7075 Using Selective Laser Melting (SLM). *Phys. Procedia* **2016**, *83*, 918–926. [CrossRef]
31. Qi, T.; Zhu, H.H.; Zhang, H.; Yin, J.; Ke, L.D.; Zeng, X.Y. Selective laser melting of Al7050 powder: Melting mode transition and comparison of the characteristics between the keyhole and conduction mode. *Mater. Des.* **2017**, *135*, 257–266. [CrossRef]
32. Otani, Y.; Kusaki, Y.; Itagaki, K.; Sasaki, S. Microstructure and mechanical properties of A7075 alloy with additional Si objects fabricated by selective laser melting. *Mater. Trans.* **2019**, *60*, 2143–2150. [CrossRef]
33. Otani, Y.; Sasaki, S. Effects of the addition of silicon to 7075 aluminum alloy on microstructure, mechanical properties, and selective laser melting processability. *Mater. Sci. Eng. A* **2020**, *777*, 139079. [CrossRef]
34. Zhou, S.Y.; Su, Y.; Wang, H.; Enz, J.; Ebel, T.; Yan, M. Selective laser melting additive manufacturing of 7xxx series Al-Zn-Mg-Cu alloy: Cracking elimination by co-incorporation of Si and TiB2. *Addit. Manuf.* **2020**, *36*, 10145. [CrossRef]
35. Aboulkhair, N.T.; Simonelli, M.; Parry, L.; Ashcroft, I.; Tuck, C.; Hague, R. 3D printing of Aluminium alloys: Additive Manufacturing of Aluminium alloys using selective laser melting. *Prog. Mater. Sci.* **2019**, *106*, 100578. [CrossRef]

36. Zhou, L.; Pan, H.; Hyer, H.; Park, S.; Bai, Y.; McWilliams, B.; Cho, K.; Sohn, Y. Microstructure and tensile property of a novel AlZnMgScZr alloy additively manufactured by gas atomization and laser powder bed fusion. *Scripta Mater.* **2019**, *158*, 24–28. [CrossRef]
37. Bi, J.; Lei, Z.L.; Chen, Y.B.; Chen, X.; Tian, Z.; Liang, J.W.; Zhang, X.R.; Qin, X.K. Microstructure and mechanical properties of a novel Sc and Zr modified 7075 aluminum alloy prepared by selective laser melting. *Mater. Sci. Eng. A* **2019**, *768*, 138478. [CrossRef]
38. Lei, Z.L.; Bi, J.; Chen, Y.B.; Chen, X.; Qin, X.K.; Tian, Z. Effect of energy density on formability, microstructure and micro-hardness of selective laser melted Sc- and Zr-modified 7075 aluminum alloy. *Powder. Technol.* **2019**, *356*, 594–606. [CrossRef]
39. Zhu, Z.G.; Ng, F.L.; Seet, H.L.; Lu, W.J.; Liebscher, C.H.; Rao, Z.Y.; Raabe, D.; Nai, S.M.L. Superior mechanical properties of a selective-laser-melted AlZnMgCuScZr alloy enabled by a tunable hierarchical microstructure and dual-nanoprecipitation. *Mater. Today* **2022**, *52*, 90–101. [CrossRef]
40. Huang, K.; Feng, Q.; Zhou, W.B.; Huang, L.; Xiang, J.; Luo, N.N.; Han, K.; Zhu, Y.T.; Wei, Y.Z. Effects of Sc addition on microstructure, mechanical and corrosion resistance properties of 7055 Al alloy. *Mater. Res. Express* **2021**, *8*, 046534. [CrossRef]
41. Vlach, M.; Cizek, J.; Kodetova, V.; Leibner, M.; Cieslar, M.; Harcuba, P.; Bajtosova, L.; Kudrnova, H.; Vlasak, T.; Neubert, V.; et al. Phase transformations in novel hot-deformed Al–Zn–Mg–Cu–Si–Mn–Fe(–Sc–Zr) alloys. *Mater. Des.* **2020**, *193*, 108821. [CrossRef]
42. Li, J.H.; Wiessner, M.; Albu, M.; Wurster, S.; Sartory, B.; Hofer, F.; Schumacher, P. Correlative characterization of primary Al_3(Sc, Zr) phase in an Al–Zn–Mg based alloy. *Mater. Char.* **2015**, *102*, 62–70. [CrossRef]
43. Deng, Y.; Yin, Z.M.; Pan, Q.L.; Xu, G.F.; Duan, Y.L.; Wang, Y.J. Nano-structure evolution of secondary $Al_3(Sc_{1-x}Zr_x)$ particles during superplastic deformation and their effects on deformation mechanism in Al-Zn-Mg alloys. *J. Alloys Compd.* **2017**, *695*, 142–153. [CrossRef]
44. Yang, Y.; Tan, P.; Sui, Y.D.; Jiang, Y.H.; Zhou, R.F. Influence of Zr content on microstructure and mechanical properties of As-cast Al-Zn-Mg-Cu alloy. *J. Alloys Compd.* **2021**, *867*, 158920. [CrossRef]
45. Samuel, A.M.; Alkahtani, S.A.; Doty, H.W.; Samuel, F.H. Role of Zr and Sc addition in controlling the microstructure and tensile properties of aluminum-copper based alloys. *Mater. Des.* **2015**, *88*, 1134–1144. [CrossRef]
46. Mikhaylovskaya, A.V.; Ghayoumabadi, M.E.; Mochugovskiy, A.G. Superplasticity and mechanical properties of Al–Mg–Si alloy doped with eutectic-forming Ni and Fe, and dispersoid-forming Sc and Zr elements. *Mater. Sci. Eng. A* **2021**, *817*, 141319. [CrossRef]
47. Mondol, S.; Kashyap, S.; Kumar, S.; Chattopadhyay, K. Improvement of high temperature strength of 2219 alloy by Sc and Zr addition through a novel three-stage heat treatment route. *Mater. Sci. Eng. A* **2018**, *732*, 157–166. [CrossRef]
48. Wang, K.X.; Yin, D.F.; Zhao, Y.C.; Atrens, A.; Zhao, M.C. Microstructural evolution upon heat treatments and its effect on corrosion in Al-Zn-Mg alloys containing Sc and Zr. *J. Mater. Res. Technol.* **2020**, *9*, 5077–5089. [CrossRef]
49. Pauly, S.; Wang, P.; Kühn, U.; Kosiba, K. Experimental determination of cooling rates in selectively laser-melted eutectic Al-^{33}Cu. *Addit. Manuf.* **2018**, *22*, 753–757. [CrossRef]
50. Bertoli, U.S.; Guss, G.; Wu, S.; Matthews, M.J.; Schoenung, J.M. In-situ characterization of laser-powder interaction and cooling rates through high-speed imaging of powder bed fusion additive manufacturing. *Mater. Des.* **2017**, *135*, 385–396. [CrossRef]
51. Bayoumy, D.; Schliephake, D.; Dietrich, S.; Wu, X.H.; Zhu, Y.M.; Huang, A.J. Intensive processing optimization for achieving strong and ductile Al-Mn-Mg-Sc-Zr alloy produced by selective laser melting. *Mater. Des.* **2021**, *198*, 109317. [CrossRef]
52. Robson, J.D. A new model for prediction of dispersoid precipitation in aluminium alloys containing zirconium and scandium. *Acta Mater.* **2004**, *52*, 1409–1421. [CrossRef]
53. Lee, Y.S.; Koh, D.H.; Kim, H.W.; Ahn, Y.S. Improved bake-hardening response of Al-Zn-Mg-Cu alloy through pre-aging treatment. *Scripta Mater.* **2018**, *147*, 45–49. [CrossRef]
54. Buha, J.; Lumley, R.N.; Crosky, A.G. Secondary ageing in an aluminium alloy 7050. *Mater. Sci. Eng. A* **2008**, *492*, 1–10. [CrossRef]
55. Berg, L.K.; Gjønnes, J.; Hansen, V.; Li, X.Z.; Knutson-Wedel, M.; Waterloo, G.; Schryvers, D.; Wallenberg, L.R. GP-zones in Al–Zn–Mg alloys and their role in artificial aging. *Acta Mater.* **2001**, *49*, 3443–3451. [CrossRef]
56. Hunt, J.D. Steady State Columnar and Equiaxed Growth of Dendrites and Eutectic. *Mater. Sci. Eng.* **1984**, *65*, 75–83. [CrossRef]
57. Spierings, A.B.; Dawson, K.; Heeling, T.; Uggowitzer, P.J.; Schäublin, R.; Palm, F.; Wegener, K. Microstructural features of Sc- and Zr-modified Al-Mg alloys processed by selective laser melting. *Mater. Des.* **2017**, *115*, 52–63. [CrossRef]
58. Yang, K.V.; Shi, Y.; Palm, F.; Wu, X.; Rometsch, P. Columnar to equiaxed transition in Al-Mg(-Sc)-Zr alloys produced by selective laser melting. *Scr. Mater.* **2018**, *145*, 113–117. [CrossRef]
59. Liu, J.; Kou, S. Crack susceptibility of binary aluminum alloys during solidification. *Acta Mater.* **2016**, *110*, 84–94. [CrossRef]
60. Sigworth, G.K.; Kuhn, T.A. Grain refinement of aluminum of aluminum casting alloys. *Int. Met.* **2007**, *1*, 31–40. [CrossRef]
61. Spittle, J.A. Grain refinement in shape casting of aluminum alloys. *Int. J. Cast Met. Res.* **2006**, *19*, 210–222. [CrossRef]